UiO **: Department of Physics**
University of Oslo

Computing the Phase Shift

Eller noe slikt

Erlend Lima

October 14, 2020

Abstract

Contents

1. Introduction

The interactions between nucleons is [fullfør] In contrast to the electromagnetic force, there is no fundamental theory of the strong force. As the quarks and gluons dance together within nuclei, their strong interaction leaks out as the residual nuclear force, binding the nucleons together. As such, the nucleon-nucleon interaction must be described by approximations and phenomenological models.

The phase shift is a useful proxy for understanding nucleon-nucleon interaction, acting as a bridge between empirically obtained cross sections and theoretical models. Among these theoretical tools to compute the phase section are the K-matrix theory and the variable phase approach (VPA). Both of these are herein investigated by applying them to a two-nucleon system, implemented in the https://julialang.org/.

2. Theory

Quantum scattering is a very complicated process, behaving so differently from the classical case of billiard balls that our intuition breaks down. Fortunately, the intricacies of the scattering process itself can be conveniently omitted by instead focusing on the relationship between the initial and resulting states, illustrated in FIGURE. Specifically, the true state $|\psi\rangle$ is related to the asymptotic incoming and outgoing states $|\psi_{\text{in}}\rangle$ and $|\psi_{\text{out}}\rangle$ through the so-called Møller operators $\Omega_\pm$:

$$|\psi\rangle = \Omega_+ |\psi_{\text{in}}\rangle = |\phi+\rangle$$
$$|\psi\rangle = \Omega_- |\psi_{\text{out}}\rangle = |\phi-\rangle.$$

[Add some history of Møller]

If time dependence is added, the Møller operations allows one to move between the asymptotic states and the actual state at time t. Combining them, the outgoing state is related to the incoming state by

$$|\psi_{\text{out}}\rangle = \Omega_-^\dagger \Omega_+ |\psi_{\text{in}}\rangle = \mathcal{S} |\psi_{\text{in}}\rangle$$

giving the definition of the scattering operator $\mathcal{S}$. In the general case let $|\chi-\rangle$ and $|\Phi+\rangle$ by any arbitrary orbits. The probability of the process $|\chi-\rangle \leftarrow |\Phi+\rangle$ occurring is then the square of the matrix element of $\mathcal{S}$:

$$w(\chi \leftarrow \Phi) = |\langle \chi - |\Phi+\rangle|^2 = |\langle \chi|\mathcal{S}|\Phi\rangle|^2.$$

The probability w is itself not observable, however, the related quantity cross-section $\sigma(\chi \leftarrow \Phi)$ is. The outgoing particle can scatter in a solid angle $d\Omega$, oriented in the direction of momentum $\vec{p}$. Likewise, the incoming particle can be described as wave packets with narrowly defined momentum $\vec{p_0}$. It can then be shown that[CITE] the differential cross section is

$$\frac{\mathrm{d}\sigma}{\mathrm{d}\Omega} = |f(\vec{p} \leftarrow \vec{p_0})|^2$$

with $f(\vec{p} \leftarrow \vec{p}_0)$ being the scattering amplitude, as known from elementary scattering theory. Note that only the magnitude of f can be obtained through the cross-section.

The next step is to relate cross-section to the scattering operator. It can be shown that $\mathcal{S}$ commutes with the free Hamiltonian $\mathcal{H}_0$

$$\mathcal{H} = \mathcal{H}_0 + V \qquad [\mathcal{H}_0, \mathcal{S}] = 0$$

Letting $|\mathrm{p}\rangle$ be the eigenvectors of $\mathcal{H}_0$ in momentum basis, we have

$$\langle \mathrm{p}'|[\mathcal{H}_0, \mathcal{S}]|\mathrm{p}\rangle = (E_{p'} - E_p)\langle \mathrm{p}'|\mathcal{S}|\mathrm{p}\rangle = 0$$

implying that $\langle \mathrm{p}'|\mathcal{S}|\mathrm{p}\rangle$ is zero except for $E_{p'} = E_p$. This leads to the form

$$\langle \mathrm{p}'|\mathcal{S}|\mathrm{p}\rangle = \delta(E_{p'} - E_p) \times \text{remainder}$$

At this point it is fruitful to define a new operator $\mathcal{R} \equiv 1 - \mathcal{S}$. $\mathcal{R}$ is the difference between the case of scattering and no scattering. It too commutes with $\mathcal{H}_0$, and so has the form

$$\langle \mathrm{p}'|\mathcal{R}|\mathrm{p}\rangle = -2\pi i \delta(E_{p'} - E_p) t(\mathrm{p}' \leftarrow \mathrm{p})$$

with the factors $-2\pi i$ and $t(\mathrm{p}' \leftarrow \mathrm{p})$ introduced for future convenience. The elements of $\mathcal{S}$ can therefore be written

$$\langle \mathrm{p}'|\mathcal{S}|\mathrm{p}\rangle = \delta(\mathrm{p}' - \mathrm{p}) - 2\pi i \delta(E_{p'} - E_p) t(\mathrm{p}' \leftarrow \mathrm{p}).$$

The first term describes the situation where no scattering occurs, while the second is the amplitude when the wave is actually scattered. The function $t(\mathrm{p}' \leftarrow \mathrm{p})$ is continuous for most potentials and analytic for many, but only defined for the "shell" $\mathrm{p}'^2 = \mathrm{p}^2$. However unphysical, it is computationally beneficial to define an operator $\mathcal{T}$ whose matrix elements $\langle \mathrm{p}'|T|\mathrm{p}\rangle$ are defined for all p and coincide with the values of t on the shell.

The scattering amplitude can be shown to be related to the on-shell $\mathcal{T}$ matrix elements as[cite]

$$f(\mathrm{p}' \leftarrow \mathrm{p}) = -(2\pi)^2 m t(\mathrm{p}' \leftarrow \mathrm{p}).$$

The elements of the scattering matrix can from this be directly related to the scattering amplitude as

$$\langle \mathrm{p}'|\mathcal{S}|\mathrm{p}\rangle = \delta(\mathrm{p}' - \mathrm{p}) - \frac{i}{2\pi m}\delta(E_{p'} - E_p)f(\mathrm{p}' \leftarrow \mathrm{p}).$$

2.1. Spherical Coordinates

Introducti

As known from elementary quantum mechanics, $\mathcal{H}^0$ commutes with the angular momentum operator $\mathcal{L}^2$ and z-axis projection $\mathcal{L}_3$. These three operators form a complete set of commuting observables. Since $\mathcal{S}$ commutes with $\mathcal{H}^0$, $\mathcal{S}$ too commutes with the aforementioned operators, and is diagonal in the common basis, namely the basis of spherical waves $\{|Elm\rangle\}$, with $E, l(l+1)$ and m being the eigenvalues for $\mathcal{H}^0$, $\mathcal{L}^2$ and $\mathcal{L}_3$ respectively. Since this basis diagonalizes $\mathcal{S}$, its matrix elements are

$$\langle E'l'm'|\mathcal{S}|Elm\rangle = \delta(E' - E)\delta_{l'l}\delta_{m'm}s_l(E).$$

$\mathcal{S}$ can be shown to be unitary, implying the eigenvalues $s_l(E)$ must have modulus one, justifying the form

$$\langle E'l'm'|\mathcal{S}|Elm\rangle = \delta(E'-E)\delta_{l'l}\delta_{m'm}\exp(2i\delta_l(E))$$

The quantity $\delta_l(E)$ is the important phase shift, an observable obtainable from both experiment and numerical calculations. It is purely real with an inherent ambiguity modulo π, as seen from

$$\exp(2i[\delta_l + n\pi]) = \exp(2i\delta_l)\exp(2in\pi) = \exp(2i\delta_l).$$

[Meaning of T in the sense incident plane wave] []

The decomposition of $f(\mathrm{p}' \leftarrow \mathrm{p})$ into partial waves can be obtained by exploiting the relation

$$\langle \mathrm{p}'|(\mathcal{S}-1)|\mathrm{p}\rangle = \frac{i}{2\pi m}\delta(E'-E)f(\mathrm{p}' \leftarrow \mathrm{p}). \qquad (2.1)$$

Inserting a complete set of states of the left hand side gives

$$\langle \mathrm{p}'|(\mathcal{S}-1)|\mathrm{p}\rangle = \int \mathrm{d}E \sum_{l,m} \langle \mathrm{p}'|(\mathcal{S}-1)|Elm\rangle \langle Elm|\mathrm{p}\rangle$$

$$= \int \mathrm{d}E \sum_{l,m} (s_l(E)-1) \langle \mathrm{p}'|Elm\rangle \langle Elm|\mathrm{p}\rangle$$

$$= \frac{1}{mp}\delta(E_{p'} - E_p) \sum_{l,m} Y_l^m(\hat{\mathrm{p}}')[s_l(E_p)-1]Y_l^m(\hat{\mathrm{p}})^*$$

where Y_l^m is the spherical harmonical and hat denotes unit vector. Combining this with (2.1), the amplitude can be decomposed to

$$f(\mathrm{p}' \leftarrow \mathrm{p}) = \frac{2\pi}{ip} \sum_{l,m} Y_l^m(\hat{\mathrm{p}}')[s_l(E_p)-1]Y_l^m(\hat{\mathrm{p}})^*$$

Letting $\hat{\mathrm{p}}$ lie along z and noting independence of m [WHY], we define

$$f(E_p, \theta) \equiv f(\mathrm{p}' \leftarrow \mathrm{p}) = \frac{1}{2ip} \sum_l (2l+1)[s_l(E_p)-1]P_l(\cos\theta)$$

This leads to the natural definition of the partial wave amplitude as

$$f_l(E) \equiv \frac{s_l(E)-1}{2ip} = \frac{\exp[2i\delta_l(\theta)]-1}{2ip} = \frac{\exp[2i\delta_l(E)]\sin\delta_l(E)}{p}$$

Analogously the total cross-section can be decomposed into partial wave cross-sections, giving

$$\sigma(p) = \sum_l \sigma_l(p) = \sum_l 4\pi(2l+1)|f_l(p)|^2 = \sum_l 4\pi(2l+1)\frac{\sin^2\delta_l}{p^2}$$

The magnitude of each partial wave cross-section is from this constrained by the so called unitary bound:

$$|\sigma_l| \le 4\pi\frac{2l+1}{p^2}.$$

The maximal value is only reached if δ_l is an odd multiple of $\pi/2$

2.2. Green's Function

One of the most important tools in scattering theory is the resolvent, or Green's operator. For many types of integral equations, a Green's function can be associated, transforming the solving of the equation to the computation of the Green's function. For our purposes the most important Green's operators are the free Green's operator

$$\mathcal{G}^0(z) \equiv (z - \mathcal{H}^0)^{-1}$$

and the full Green's operator

$$\mathcal{G}(z) \equiv (z - \mathcal{H})^{-1}$$

with $z \in \mathbb{C}$. Without loss of generality, assume the spectrum of $\mathcal{H}$ is discrete, with the orthonormal basis $|n\rangle$. Then the full Green's operator can be written

$$\mathcal{G}(z) = (z - \mathcal{H})^{-1} 1 = \sum_n \frac{|n\rangle\langle n|}{z - E_n}.$$

A specific matrix element is therefore

$$\langle\chi|\mathcal{G}(z)|\psi\rangle = \sum_n \frac{\langle\chi|n\rangle\,\langle n|\psi\rangle}{z - E_n}.$$

For any z not an eigenvalue E_n, the matrix element is well defined and analytic. When z is an eigenvalue, it is a simple pole with residue $\langle\chi|n\rangle\,\langle n|\psi\rangle$. That is, knowing the poles of $\mathcal{G}(z)$ gives information about the corresponding eigenvectors. As both the energy eigenvectors and eigenvalues can be found from $\mathcal{G}(z)$ itself, knowledge of $\mathcal{G}(z)$ is equivalent to solving the eigenvalue problem of $\mathcal{H}$[*].

While discrete spectra lead to poles in $\langle\chi|\mathcal{G}(z)|\psi\rangle$, continuous spectra lead to branch cuts. Consider the free Green's operator, which in terms of the angular momentum eigenvectors in analogy to the discrete spectrum has the matrix elements

$$\langle\chi|\mathcal{G}^0(z)|\psi\rangle = \int_0^\infty \frac{\mathrm{d}E}{z - E} \left\{ \sum_{l,m} \langle\chi|Elm\rangle\,\langle Elm|\psi\rangle \right\}$$

which again gives well-defined functions for $z \notin \mathbb{R}^+$. For any $E^0 > 0$, the integral diverges. This can be seen by taking the difference between approaching the axis from the top and approaching it from the bottom, which can be shown to yield $2\pi i \sum_{lm} |Elm\rangle\langle Elm|$.

The scattering process can yield both scattered states and bound states. The former is associated with continuous spectra while the latter with discrete. From the discussion above, scattered states are associated with branch cuts along $E^0 > 0$ while bound states show up as simple poles in $\mathcal{G}(z)$.

Finding $\mathcal{G}(z)$ is just as difficult as solving the eigenvalue problem for $\mathcal{H}$. Using $\mathcal{G}(z)$, however, yields an alternative numerical approach while at the same providing a powerful theoretical tool. The first step is to write $\mathcal{G}(z)$ in terms of the simpler $\mathcal{G}^0(z)$. This is trivially done using the algebraic relation

---

[*]Of course, this is merely an intuitive explanation, not a proof. It can be shown that this is indeed true in the general case.

$$\mathcal{A}^{-1} = \mathcal{B}^{-1} + \mathcal{B}^{-1}(\mathcal{B} - \mathcal{A})\mathcal{A}^{-1}.$$

Inserting $\mathcal{A} = z - \mathcal{H}$ and $\mathcal{B} = z - \mathcal{H}^0$ gives

$$\mathcal{G}(z) = \mathcal{G}(z)^0 + \mathcal{G}(z)^0 V \mathcal{G}(z) = \mathcal{G}(z)^0 + \mathcal{G}(z)V\mathcal{G}(z)^0. \tag{2.2}$$

This is known as the Lippmann-Schwinger equation for $\mathcal{G}(z)$.

2.3. Lippman Schwinger

The Lippmann-Schwinger equation turns out to be a common and useful relation between operators in scattering theory. The derivation through Green's operators is not the historic path, and has the downside of obscuring its physical relationship to the Schrödinger equation. [Mer historie]

[intro] Out of thin air we define the operator $\mathcal{T}$ as the potential plus the distortion to the potential caused by the full Green's operator:

$$\mathcal{T}(z) = V + V\mathcal{G}V. \tag{2.3}$$

It is clear that $\mathcal{T}(z)$ has the same properties as $\mathcal{G}(z)$ with respect to poles and branch cuts. Combining (2.3) with (2.2) together with some algebraic manipulations, we obtain the Lippmann-Schwinger equation for $\mathcal{T}(z)$:

$$\mathcal{T}(z) = V + V\mathcal{G}^0(z)\mathcal{T}(z). \tag{2.4}$$

In momentum space (2.4) is written as

$$\langle \mathrm{p}'|\mathcal{T}(z)|\mathrm{p}\rangle = \langle \mathrm{p}'|V|\mathrm{p}\rangle + \int \mathrm{d}^3 p'' \frac{\langle \mathrm{p}|V|\mathrm{p}''\rangle}{z - E_{p''}} \langle \mathrm{p}''|T(z)|\mathrm{p}\rangle$$

This highlights the need for introducing the $\mathcal{T}$ operator in the first place. There is no LS equation for the $\mathcal{S}$ because it requires the operators to be smooth functions, while $\mathcal{S}(z)$ is highly singular. On the other hand $\mathcal{T}$ analytic almost everywhere, allowing it to be expressed in terms of an integral equation.

Through a long and rather limit-finicky derivation, the $\mathcal{S}$ operator can be derived in terms of the $\mathcal{T}$ operator when z approaches the real axis from above

$$\langle \mathrm{p}'|S|\mathrm{p}\rangle = \delta(\mathrm{p}' - \mathrm{p}) - 2\pi i \delta(E_{p'} - E_p) \lim_{\epsilon \downarrow 0} \langle \mathrm{p}'|T(E_p + i\epsilon)|\mathrm{p}\rangle.$$

This relation being the main motivation for defining $\mathcal{T}$ in the first place. It shows that $t(\mathrm{p}' \leftarrow \mathrm{p})$ corresponds to the on-shell T-matrix.

A reasonable question to ask is why computing the entire T-matrix is necessary when only the on-shell elements are physical. As already mentioned, one reason is computational; The on-shell elements are the limiting quantities of the off-shell elements. This doesn't mean that the off-shell elements are only a mathematical necessity. In fact, they correspond to the virtual interactions in the scattering process, which accounts for their fundamental unmeasurable

nature. We are only allowed to observe the scattering in the non-interacting region, being the limiting case of the unobservable processes happening inside of the interacting region. Our initial starting point of focusing on the asymptotic states while ignoring the intricacies of the scattering is therefore not some mathematical trick to make computation easier, but an unavoidable requirement.

2.4. The K-Matrix

The Lippmann-Schwinger equation for $\mathcal{T}$ can not be solved by simple analytical methods. One recourse is to use approximation techniques. These are based on the expansion of $\mathcal{T}$ into the infinite sum

$$\mathcal{T} = V + V\frac{1}{E - H^0 + i\epsilon}V + V\frac{1}{E - H^0 + i\epsilon}V\frac{1}{E - H^0 + i\epsilon}V + ...$$

The unitarity condition of $\mathcal{T}$ is satisfied for the whole series, but violated for any finite order. If the series happens to be rapidly convergent, it may not pose a problem for numerical methods[†]. Nevertheless, a more stable approach is to enforce unitarity. The Caley transform achieves this, whereby a operator is constructed in such a way as to ensure unitary.

The Caley transform of $\mathcal{S}$ is denoted by $\mathcal{M}$, and is defined as

$$\mathcal{M} = i\frac{1 - \mathcal{S}}{1 + \mathcal{S}}.$$

The K-matrix[‡] is the matrix elements of the $\mathcal{M}$ operator:

$$\langle \mathrm{p}'|\mathcal{M}|\mathrm{p}\rangle = \delta(E_{p'} - E_p)k(\mathrm{p}' \leftarrow \mathrm{p}).$$

When $\mathcal{S}$ is symmetric, $\mathcal{M}$ is both Hermitian and symmetric, implying its matrix elements are real. As with $\mathcal{S}$ and $\mathcal{R}$, $\mathcal{M}$ becomes diagonal in the basis $\{|Elm\rangle\}$:

$$\langle E'l'm'|\mathcal{S}|Elm\rangle = \delta(E_{p'} - E_p)\delta_{l',l}\delta_{m',m}s_l(E)$$
$$\langle E'l'm'|\mathcal{R}|Elm\rangle = \delta(E_{p'} - E_p)\delta_{l',l}\delta_{m',m}2ipf_l(E)$$
$$\langle E'l'm'|\mathcal{M}|Elm\rangle = \delta(E_{p'} - E_p)\delta_{l',l}\delta_{m',m}k_l(E).$$

The elements $k_l(E)$ will in this case be real, and are directly related to the phase shifts:

$$k_l = i\frac{1 - s_l}{1 + s_l} = \tan\delta_l.$$

[fix factor 1/p]

It can be shown that in the same way as $\mathcal{S}$ is related to expansion into plane wave stationary states $|\mathrm{p}\pm\rangle$, $\mathcal{M}$ is related to expansion into standing waves $|\mathrm{p}s\rangle$

[Expand a bit on standing waves]

[Derive Heitler's equation]

[†]That is to say, if the process described is sufficiently inelastic, energy will be approximately conserved. [1]

[‡]The nomenclature of the K-matrix is a mess. It is also called the R-matrix, the T-matrix, the reaction matrix, the reactance matrix, the dampening matrix, the distortion matrix, the dissipative matrix, and Heitler's matrix. To avoid overworking any of the other letters, I follow the style of Taylor.

2.5. Bound States and Levinson's Theorem

[The Jost function] [Poles of S] [Levinson]

2.6. Potentials

2.6.1. The Square Well

Near and dear to everyone is the square well potential; a simple discontinuous potential with value V_0 in the interacting region and zero everywhere else:

$$V(r) = \begin{cases} V_0 & \text{for } 0 \leq r \leq R \\ 0 & \text{for } r > R \end{cases}$$
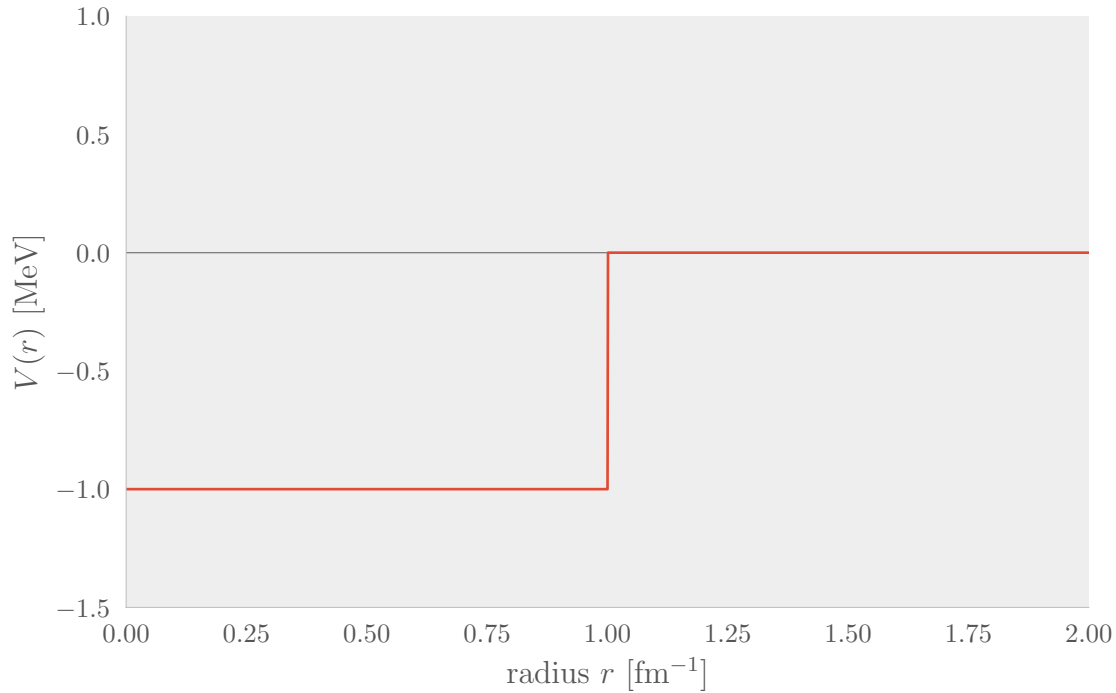
The potential is plotted in Fig. 2.1

Figure 2.1: An attractive square well potential with $V_0 = -1$ MeV.

[Analytical Solutions]

2.6.2. The Yukawa Potential

[HISTORY]

The Yukawa potential was later generalized into a class of generalized Yukawa potentials. They are potentials build on superpositions of Yukawa potentials:

$$V(r) = \sum_{i=1}^{N} C_i \frac{e^{-\eta_i r}}{r}$$

for some coefficients C_i and η_i.

A specific instance of a generalized Yukawa potential is the Reid potential[2]. It was an incremental improvement on already existing potentials at that time, building a parameterized potential where the exponent in each term reflects some phenomenological properties of the nuclear force while the constants are fit to phase shift data without consideration for their physical interpretation. In the case of proton-neutron scattering, the potential for the partial wave $^1S_0$ consists of the three terms:

$$V(r) = V_a \frac{e^{-ax}}{x} + V_b \frac{e^{-bx}}{x} + V_c \frac{e^{-cx}}{x}$$

where $x = \mu r$, $\mu = 0.7$ MeV, $V_a = -10.463$ MeV, $V_b = -1650.6$ MeV, $V_c = 6484.3$ MeV, and $a = 1$, $b = 4$ and $c = 7$.

The individual terms are plotted in Fig. 2.2 along with their sum. Its construction becomes apparent, where the three terms interact to form its three main features: it is a short range potential, quickly falling off to zero with a range , with an attractive region followed by a strongly repulsive region.
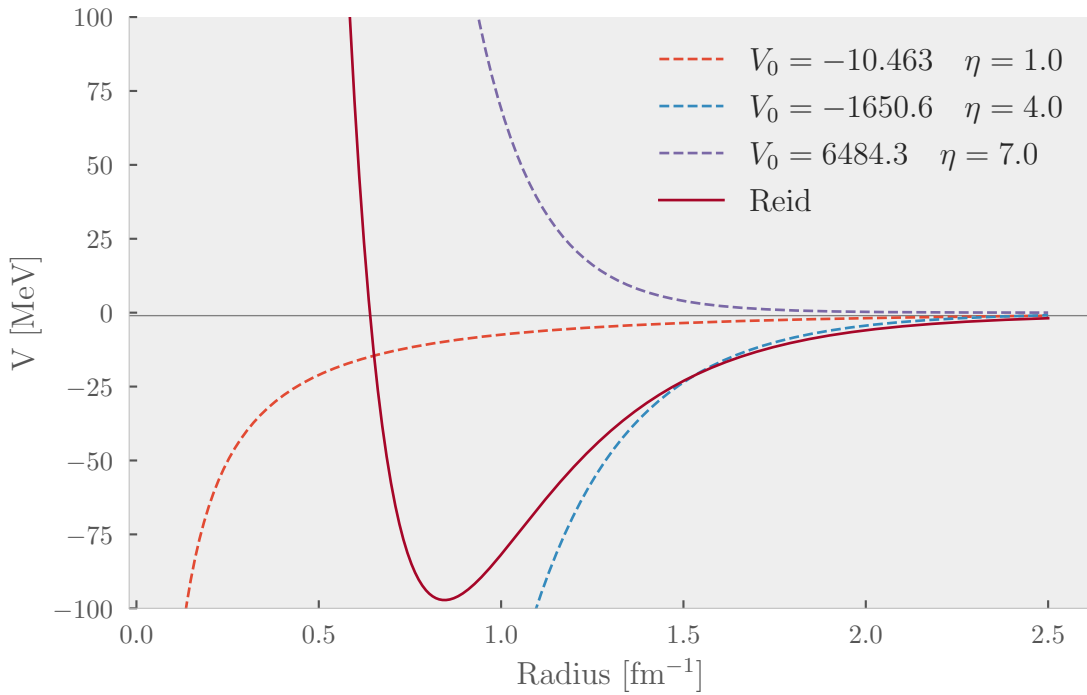

Figure 2.2: The Reid potential (full stroke), a sum of three Yukawa potentials (dashed). It is has the typical characteristics of a nuclear force model, with a short range attractive potential followed by a repulsive core.

The Reid potential for np $^1S_0$ was fit to two thousand data points for the phase shift in the region $0-350$ MeV, and thus should provide a good fit in this region.

2.6.3. Momentum Basis

Going from position basis to momentum space requires a change of basis, achieved through a Fourier transform. The problem is multidimensional, requiring a generalized Fourier trans-

form. As we are only dealing with spherically symmetric and central potentials, the more suitable Hankel transform§ can be used. For s-waves, it takes the form:

$$V_l(k, k') = \int_0^\infty j_0(kr) V(r) j_0(k'r) r^2 \mathrm{d}r.$$

[Square well in momentum basis]

[Reid in momentum basis]

3. Method

3.1. Discretizing Lippman-Schwinger

The equation [REF] can be solved numerically by iteration. To this end it is discretized through a series of steps. The principal value poses a problem due to the limited precision of computers. To step around this, the integral is rewritten. The function $\frac{1}{k-k_0}$ is even about k_0, hence having parts of the curve above and below the x-axis, meaning

$$\int_{-\infty}^\infty \frac{\mathrm{d}k}{k - k_0} = 0.$$

Breaking the integral into its positive and negative parts and performing the substitution $k \to -k$ in the negative part then yields

$$\int_0^\infty \frac{\mathrm{d}k}{k^2 - k_0^2} = 0$$

The principal value can now be expressed as

$$\mathcal{P} \int_0^\infty \frac{f(k)}{k^2 - k_0^2} \mathrm{d}k = \int_0^\infty \frac{f(k) - f(k_0)}{k^2 - k_0} \mathrm{d}k$$

The integral is no longer singular at k_0, instead being proportional to $\frac{\mathrm{d}f}{\mathrm{d}k}$, allowing it to be computed numerically.

In particular, [REF] can be recast to the form

$$K(k, k') = V(k, k') + \frac{2}{\pi} \int_0^\infty \mathrm{d}q \frac{q^2 V(k, q) K(q, k' - k_0^2 V(k, k_0) K(k_0, k')}{(k_0^2 - q^2)/m}$$

The integral is approximated through

$$\int_{-1}^1 f(x) \mathrm{d}x \approx \sum_{i=1}^N f(x_i) w_i$$

---

§The Hankel transform can be regarded as the Fourier transform in hyperspherical coordinates, expanding the function in Bessel functions instead of sines and cosines.

Listing 1 The main loop of the K-matrix method.

```
1   function createA(V, k, ω, m)
2       N = length(k)-1
3       k₀ = k[end]
4       A = diagm(0 ⇒ repeat([1.0,], N+1))
5       uⱼ = 0.0
6
7       @inbounds for j in 1:N+1
8           uⱼ = 0.0
9           if j ≠ N+1
10              uⱼ = 2/π * ω[j]*k[j]^2/((k₀^2 - k[j]^2)/m)
11          else
12              for n in 1:N
13                  uⱼ += ω[n]*k₀^2/((k₀^2 - k[n]^2)/m)
14              end
15              uⱼ *= -2/π
16          end
17
18          for i in 1:N+1
19              A[i, j] -= V[i, j] * uⱼ
20          end
21      end
22      return A
23  end
```

for N lattice points through the corresponding weights w_i and points $x_i \in [-1, 1]$. This is done through Gaussian-Legendre quadrature, using Legendre polynomials to construct the weights and corresponding points. To map the integral from $[-1, 1]$ to $[0, \text{inf}]$, the points and weights are transformed by

$$k_i = C \times \tan\frac{\pi}{4}(1 + x_i)$$

$$w_i = C \times \frac{\pi}{4}\frac{w_i}{\cos^2\left(\frac{\pi}{4}(1 - x_i)\right)}$$

where C is a constant to fix the units.

Applied to our problem, it is discretized into

$$K(k, k') = V(k, k') + \frac{2}{\pi}\sum_{i=1}^{N}\frac{w_j k_j^2 V(k, k_j) K(k_j, k')}{(k_0^2 - k_j^2)/m} - \frac{2}{\pi}k_0^2 V(k, k_0) K(k_0, k')\sum_{n=1}^{N}\frac{w_n}{(k_0^2 - k_n^2)/m}.$$

There are $N \times N$ unknowns for $K(k, k')$, plus 1 for $K(k_0, k_0)$, for a total of $N+1$ unknowns. They can be described by a single extended K-matrix. Defining another matrix A as

$$A_{i,j} = \delta_{i,j} - V(k_i, k_j)u_k$$

with

$$u_j = \frac{2}{\pi}\frac{w_j k_j^2}{(k_0^2 - k_j^2)/m} \qquad \text{for } j = 1, 2, ..., N$$

$$u_{N+1} = -\frac{2}{\pi}\sum_{j=1}^{N}\frac{k_0^2 w_j}{(k_0^2 - k_j^2)/m}.$$

The implementation of this main loop is shown in Section 3.1

The equation can now be rendered as the matrix equation

Listing 2 Implementation of VPA in Julia

```julia
struct VPA <: Method
  rspan::Tuple{Float64, Float64}  # Range of the interaction
end
VPA() = VPA((1e-4, 15.0))


function (vpa::VPA)(k, m, V::Potential)
    m = m/2

    function dδdr(δ, p, r)
      -1.0/k * 2.0m * V(r) * sin(k*r + δ)^2
    end

    δ0 = 0.0

    prob = ODEProblem(dδdr, δ0, vpa.rspan)
    sol = solve(prob, maxiters=10000, reltol=1e-8)

    δ = sol.u[end]
end
```

$$AK = V.$$

Solving for K then simply amounts to inverting A and computing the product

$$K = A^{-1}V. \tag{3.1}$$

As known from [REF], the diagonal of K is proportional to the phase shift

$$K(k_{N+1}, k_{N+1}) = K(k_0, k_0) = -\frac{1}{mk_0} \tan \delta_0(k_0)$$

The number of mesh points N controls both the accuracy and the computation resources, demanding more memory and time as N increases. Running over the $(N + 1) \times (N + 1)$ matrices scales as roughly $\mathcal{O}(N + 1)^2$ in both time and memory allocation. This is the expected behavior to compare to when measuring its actual resource usage.

3.2. Variable Phase Approach

In contrast to the LS approach, implementing the variable phase approach is straightforward. Julia has a very good differential equations solver DifferentialEq.jl[3], which is used for the actual computation. Since the limit in the relation $\delta(k) = \lim_{\rho \to \infty} \delta(k, \rho)$ can not be taken to infinity on a computer, ρ is instead substituted with a very large number, like 5. There is a trade-off between accuracy and computation time, with smaller ρ giving lesser accuracy while taking shorter time to compute, assuming the same step length is being used. To find the optimal ρ, several values were tried and the result compared to a high ρ.

The code implementation is shown in Listing 2

3.3. The Potentials

Two potentials are examined: the square well and the Reid potential. The former has analytical solutions and is relatively simple to understand, and will be used as a check on the implementation of the methods and to illustrate concepts discussed in the theory.

The latter is more complicated, being a sum of three Yukawa potentials with the intent on modeling NN-interactions, with coefficients fitted to data.

Their precise implementation is not interesting, but is available in the file potentials.jl.

4. Results and Discussion

4.1. The Square Well Potential

The square well has an analytical form for the phase shift which can be compared to the result of VPA. A well with the arbitrary depth of 4 MeV is used as example, with the computed curves shown in Fig. 2.1. The curves overlap, but the analytical solution has a jump at ≈ 2.8 MeV, stemming from the inherent modulo π ambiguity. The transformation $k \cot \delta$ lifts this ambiguity while fixing the phase shift to 0 at $k = 0$, plotted in the lower panel of the figure. Once transformed the curves overlap perfectly, as expected.

The simple form the square well potential allows us to illustrate some general behaviors of the phase shift. The phase shifts produced by several different well depths are plotted in Fig. 4.2 together with the corresponding cross sections in the lower panel. As $k \to 0$, all curves approach an integral multiple of π, and decrease towards zero as $k \to \infty$. As Levinson's theorem dictates, the multiple of π corresponds to the number of bound states each well can contain, with the number of states increasing as the potential depth increases.

For some particular well depths, the cross sections shot up beyond the limits of the plot. The phase shift curves too have a characteristic shape, rising rapidly near $k = 0$. Examples are marked by dashed lines. Such curves indicate that the potential is on verge of allowing for an additional bound state. [cont]

A related phenomenon happens where the phase shift crosses $\delta = \pi$, at which point the cross section falls off to zero. This is more clearly demonstrated in Fig. 4.3. A phase shift of $n\pi$ means the wave inside the well has precisely n more oscillations than the free wave. When the scattered wave exits the potential, it is exactly in phase with the free wave, and hence indistinguishable. If the higher $l > 0$ waves are negligible in the same region, the potential causes no scattering at all. This is the cause for the Ramsauer-Townsend effect[4, p. 195], where certain gases are completely transparent for electrons at a given energy.

For completeness sake, the phase shift is found for positive wells, see Fig. 4.4. We expect there to be no bound states, and for the phase shift to be negative. This is indeed the case, as the figure shows. The step-like behavior is due to the [cont. Skip this section? Kinda obvious. Well, the step behavior is not, but is also not interesting.].

4.2. The Reid Potential

4.2.1. K-Matrix

The phase shifts for the $^{1}S_{0}$ partial wave of np-scattering obtained through the K-matrix method is shown in Fig. 4.5. This is compared to experimental data from the Nijmegen group[5], also shown in the same figure. There is generally a good agreement, with all features of the experimental data being replicated; a rapid rise from 0 to $\approx 60°$, followed by a fall and a sign flip at ≈ 250 MeV. However, the computed phase shift is consistently lower than the experimental, until they cross.
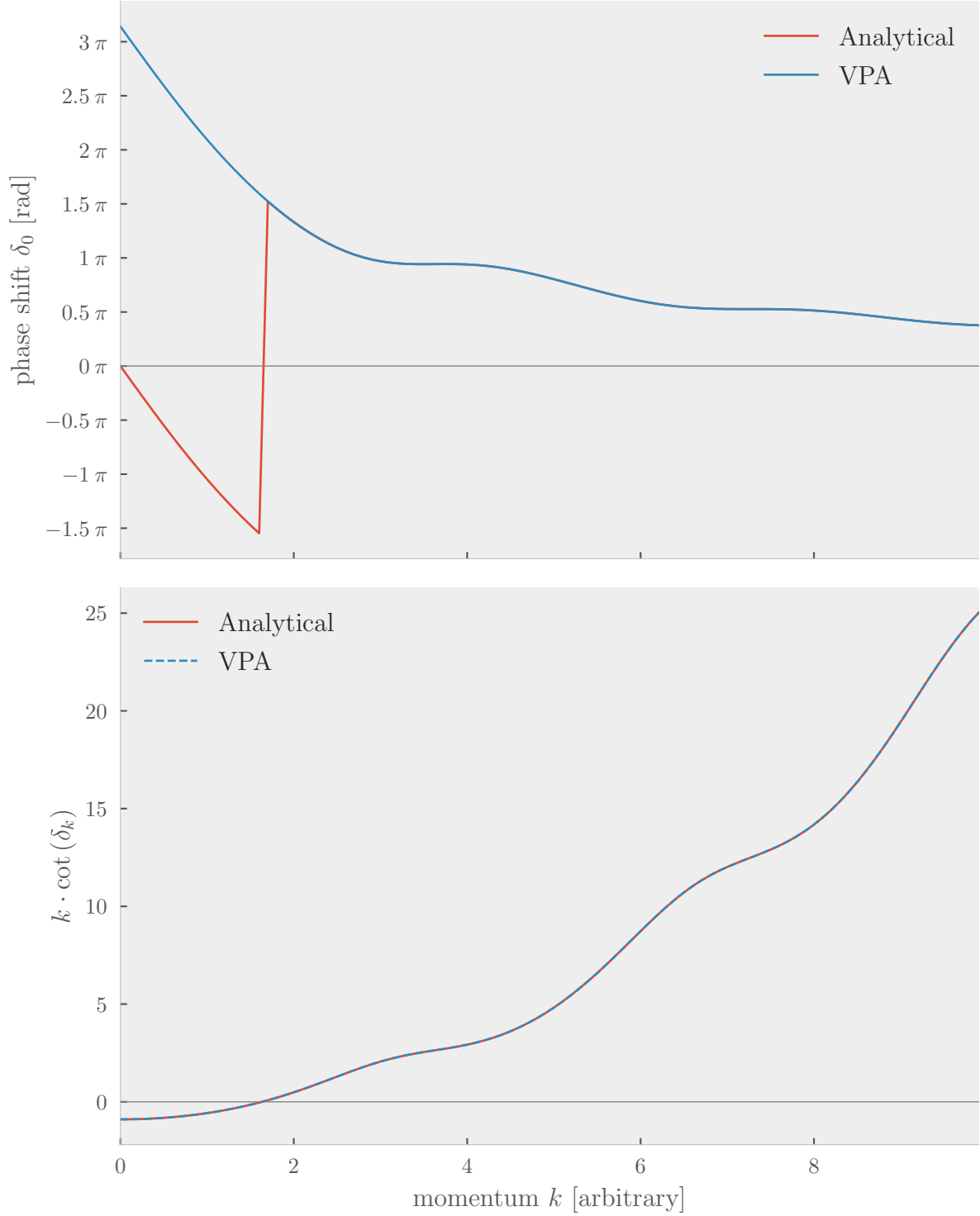
Figure 4.1: The S-wave phase shift for a square well potential $V = -4$ MeV, and reduced mass of 1 MeV. The π-ambiguity in the analytical solution is lifted in the lower panel with the transformation $k\cot\delta_0$, showing a perfect overlap.

The accuracy of the K-matrix calculations depends on the number of mesh points used. To determine its influence, the Nijmegen data was interpolated with linear interpolation, and compared to K-matrix calculations using different mesh sizes. The comparison was made by taking the total mean square error (MSE). See Fig. 4.6. As the shape of the curve remains
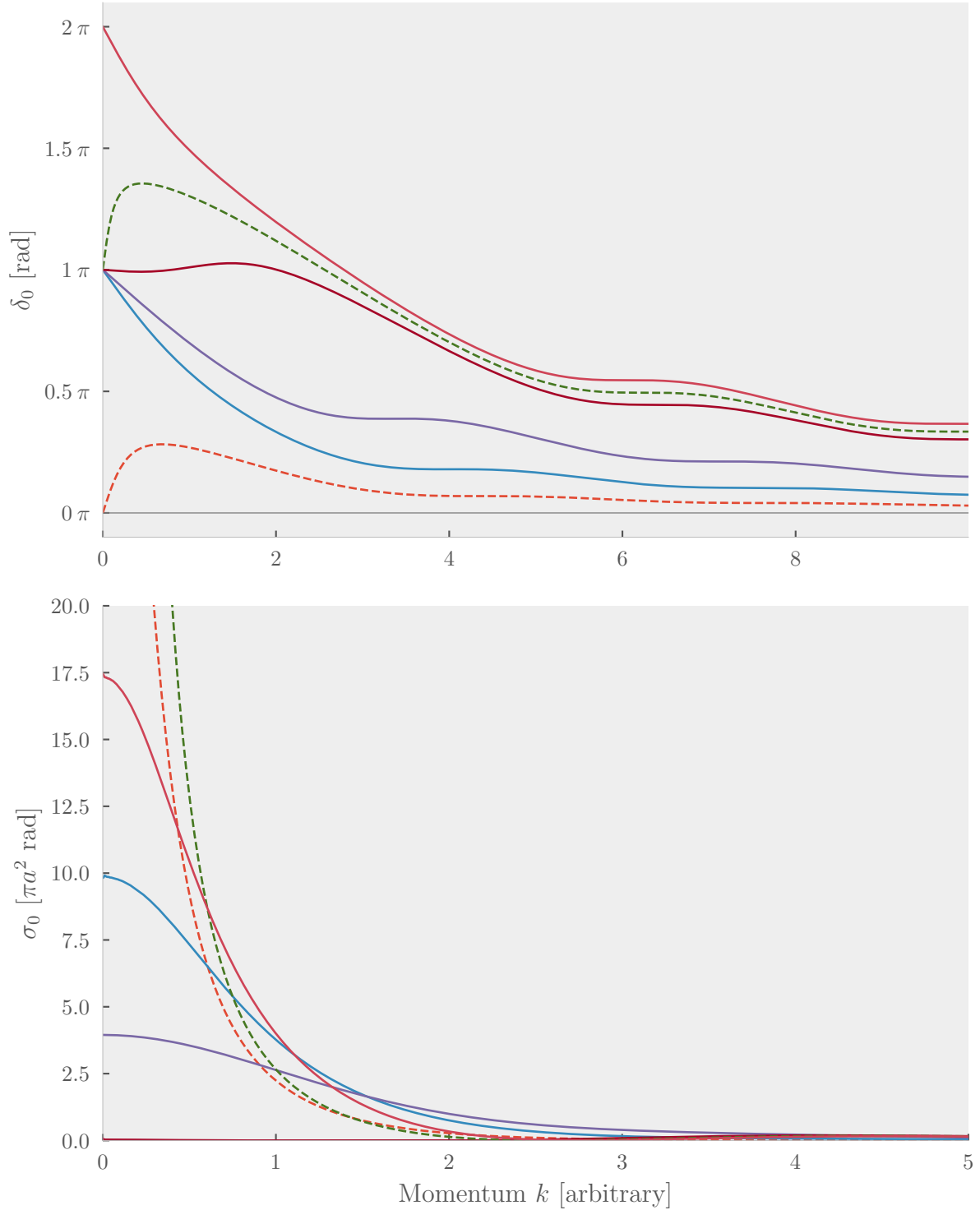
Figure 4.2: The phase shift and corresponding cross section for several square wells of different depths. All curves fall off to zero due to the potential becoming negligible. As the wells deepen, the number of possible bound states increases, manifesting as curves starting at multiples of π. The dashed lines show the zero energy peaks.
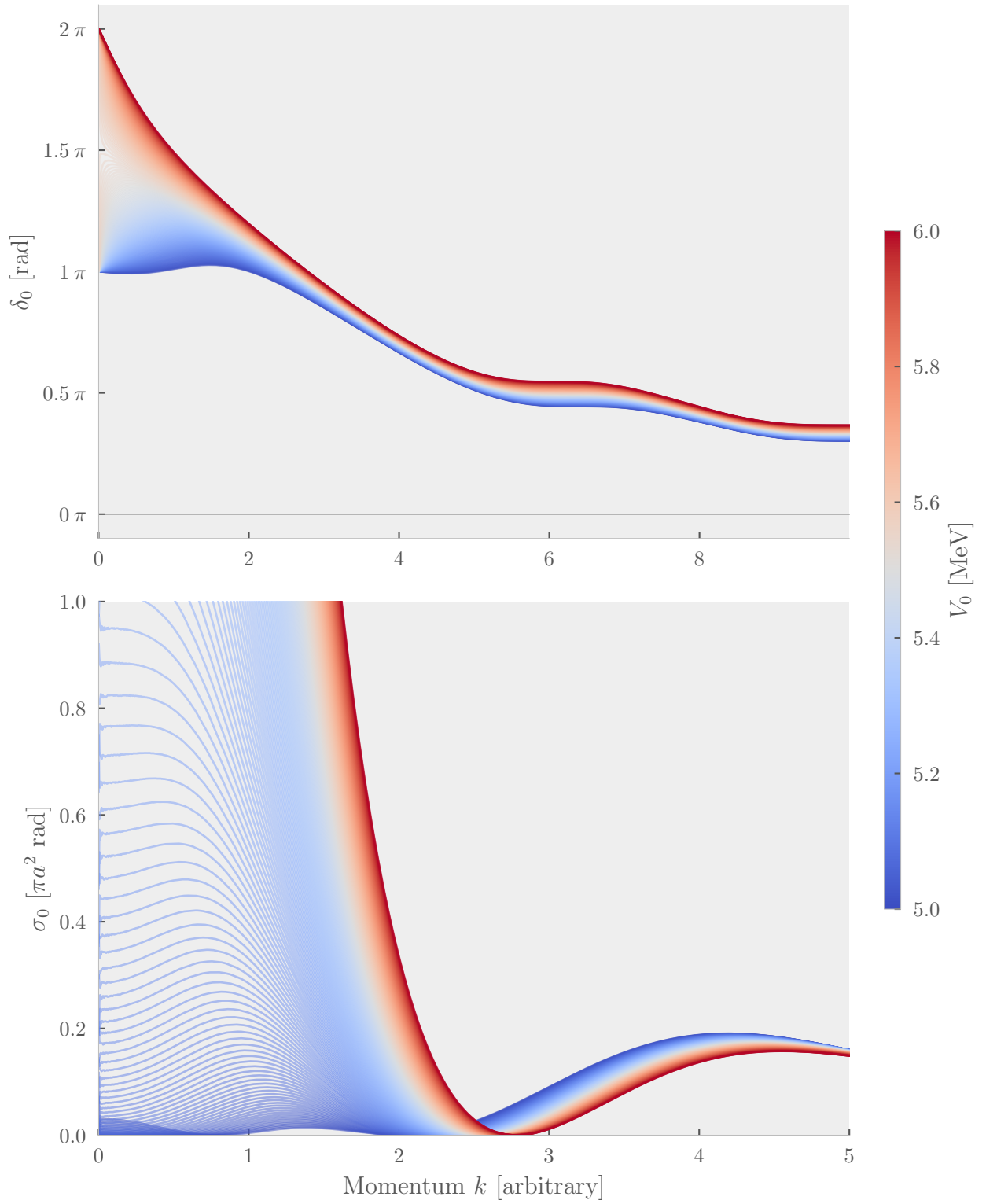
Figure 4.3: Examples of phase shift curves crossing $\delta = \pi$. The scattered wave gets in phase with the free wave, hence equivalent with no scattering. The cross section therefore plummets to zero, as is apparent.
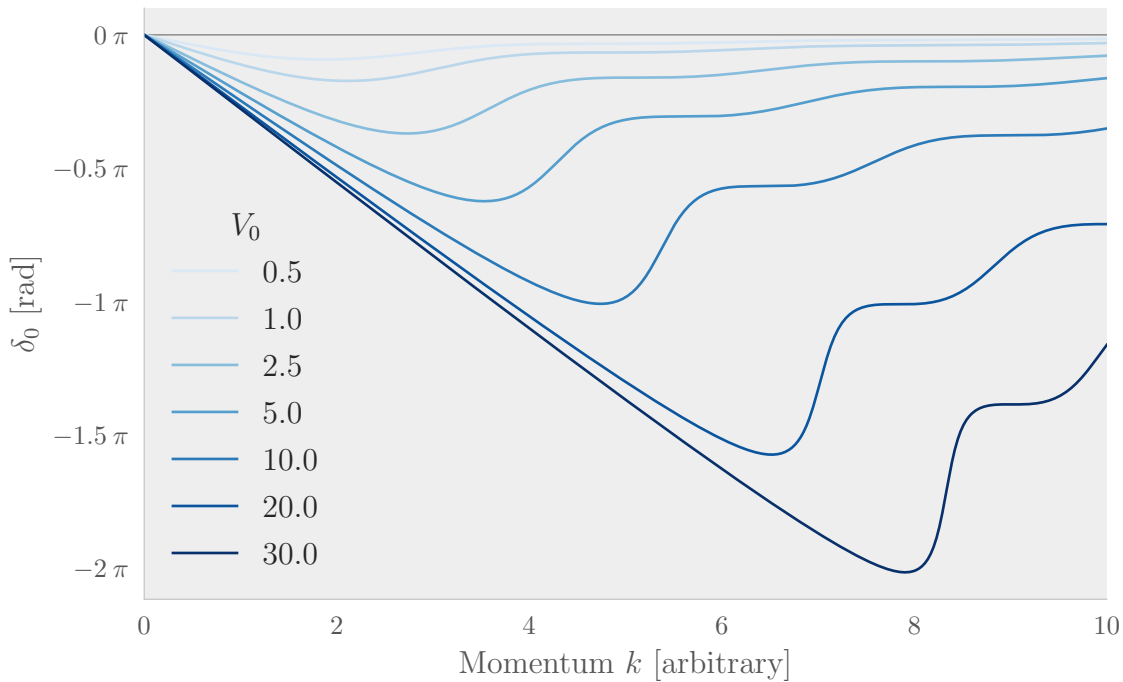
Figure 4.4: The square well with positive well depths, yielding negative phase shifts and no bound states.

fairly consistent, the MSE of the region $0 \leq T_{\text{lab}} \leq 150$ MeV was chosen as representative of the "total" MSE. This is mainly done to avoid the crossing which slightly complicates the error comparison.

Unsurprisingly, the MSE starts off jumping before quickly falling off to a minimum at about 25 mesh points. As the MSE converges with just a few mesh points, the discrepancy observed in Fig. 4.5 can not be attributed to the method itself. Increasing the number further gives negligible improvements. There is, however, an increasing cost in computational resources.

The total computation time and amount of allocated bytes used by the K-matrix method is shown in Fig. 4.7. As discussed in Section 3.1, both the time and the memory is expected to increase by roughly $\mathcal{O}(N^2)$. Fitting second degree polynomials, we see that this is indeed roughly the case, with the required time being slightly chaotic. The time was measured by repeating each calculation ten times and taking the median.

There is therefore a trade off between the resources required for a calculation and the accuracy obtained, a trade off which quickly gets increasingly poor, as no further benefit is obtained after ≈ 25 mesh points.

4.2.2. VPA

The second method for obtaining the phase shift from the Reid potential is the variable phase approach. The results are compared with the Nijmegen data in Fig. 4.8, and not unexpectedly, it gives very similar results as Fig. 4.5.
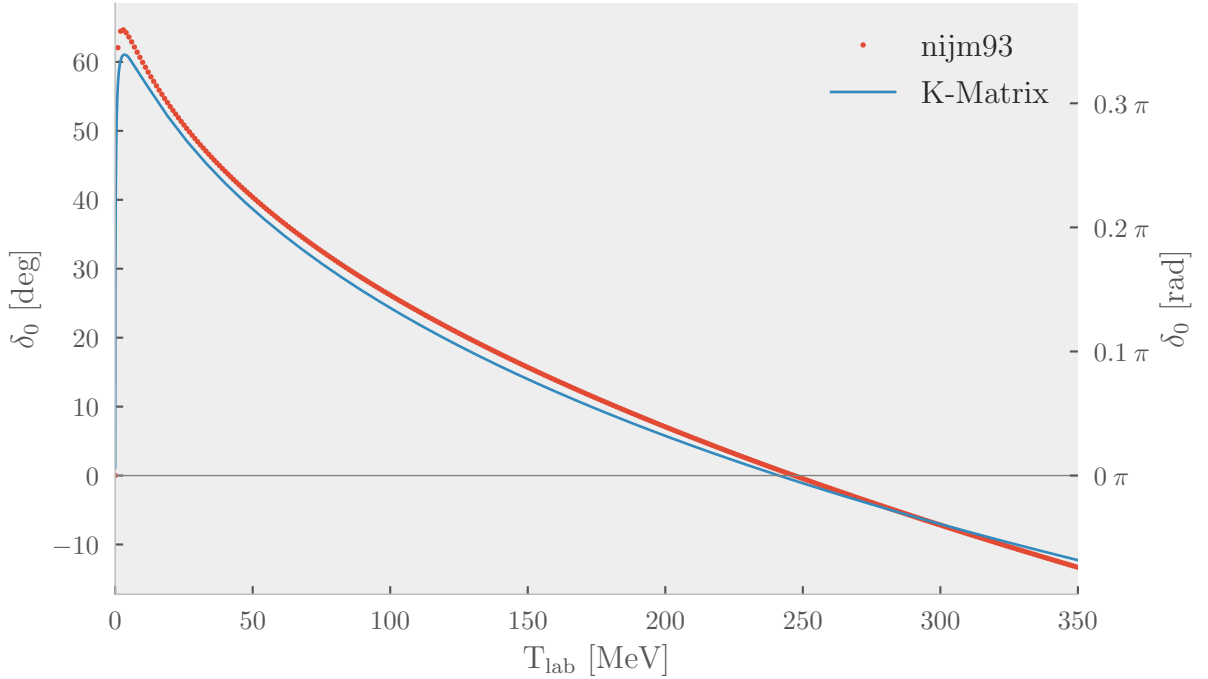
Figure 4.5: Phase shift for $^1S_0$ partial wave of np-scattering, both experimental data from[5] ($nijm$93) and from K-matrix calculations. There is good agreement, but the calculated phase shift is consistently lower than the experimental values. 30 mesh points were used in the calculation for each phase shift point.

VPA requires the cut-off of the potential to be sufficiently close to infinity to make the error negligible. Cutting off too quickly can be computationally beneficial, so there is one more a trade off between accuracy and resource usage. The resulting phase shifts from different cut-off points are shown in Fig. 4.9. When the cut-off is too small, the potential is effectively a repulsive potential, hence giving a negative phase shift. The phase shift gets increasingly negative as the interaction "sees" more of the repulsive region, but once the attractive region is included, the phase shift quickly increases and converges to the far-away solution ($r_{\text{end}} = 15$).

The resource usage of VPA is significantly more difficult to measure, as the differential equation is solved by the external package DifferentialEq.jl, allowing for a range of different parameters and methods. For completeness sake, the MSE, time and memory usage as a function of the step size is shown in the appendix Fig. A.1. The interesting information is that the time is nearly constant at ≈ 0.2 seconds for the same number of phase shift points as the K-matrix method solved in Fig. 4.7. The K-matrix method is therefore significantly faster, with no loss in accuracy.

4.2.3. Comparison & Exploration

The phase shift from both K-matrix calculations and VPA are plotted together in Fig. 4.10 alongside the experimental data. The pointwise relative error is shown in the lower panel, having a parabolic shape. The theoretical points are perfectly overlapping. Since we already
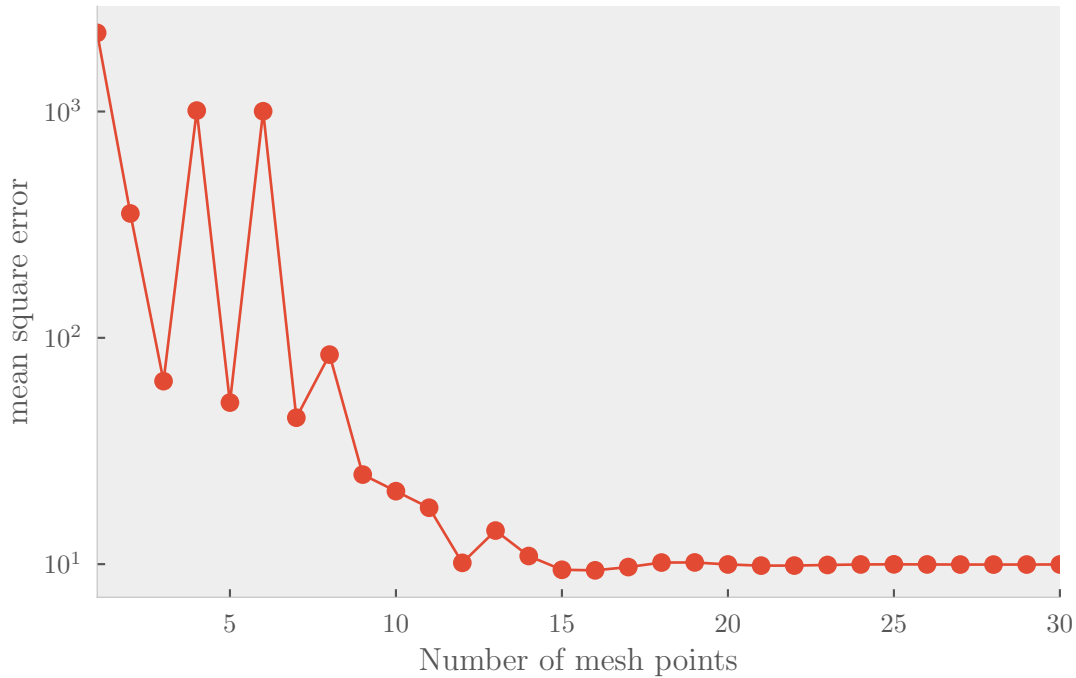
Figure 4.6: The accuracy of the K-Matrix method as a function of number of mesh points. For $n > 20$, the error remains near constant. 150 phase shifts were calculated for energies $0 \leq T_{\text{lab}} \leq 150$.

know that VPA is in agreement with the analytical solutions of the square well, we have confidence that the K-matrix method too is correctly implemented.

As the discrepancy between the theoretical computations and the experimental data can be attributed to neither the parameters of the methods nor the methods themselves, the culprit must be the model. The Reid potential was fitted to np-scattering data from the 60s and earlier, while the Nijmegen data is more complete and obtained from more accurate methods.

The phase shift curve of the Reid potential has a striking resemblance to the dashed curves of Fig. 4.2. From our earlier discussion, it is easy to suspect there to be a bound state if the potential was just slightly more attractive. To examine this, the second term of the Reid potential was increased by a few percent, yielding the phase shift curves of Fig. 4.11. At $+3.37\%$ its strength, the phase shift at $k = 0$ jumps up to 180°, allowing for a bound state by Levinson's theorem.
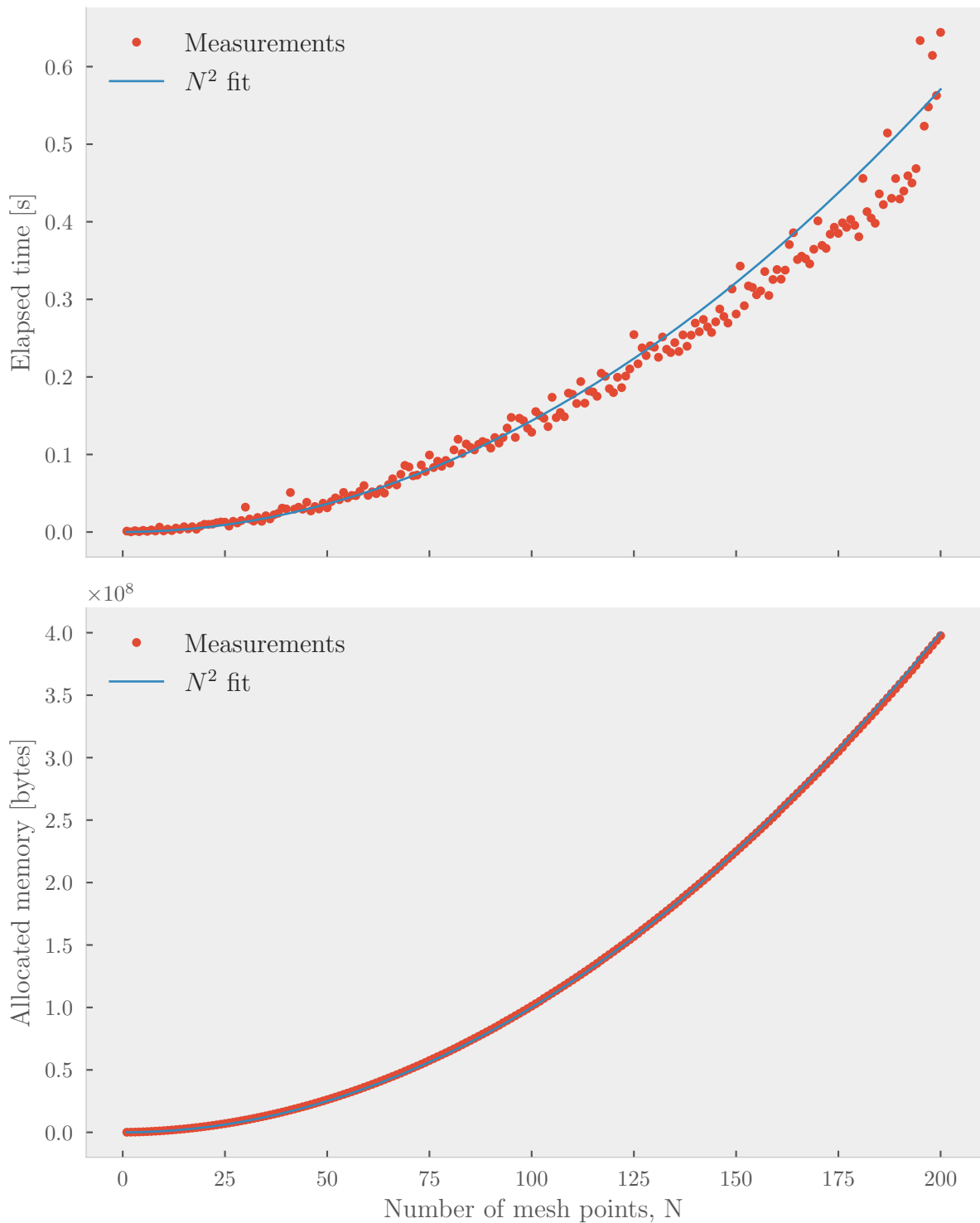
5. Conclusion

Figure 4.7: Resource usage of the K-matrix method as a function of number of mesh points. The time shows the median of 10 repetitions.
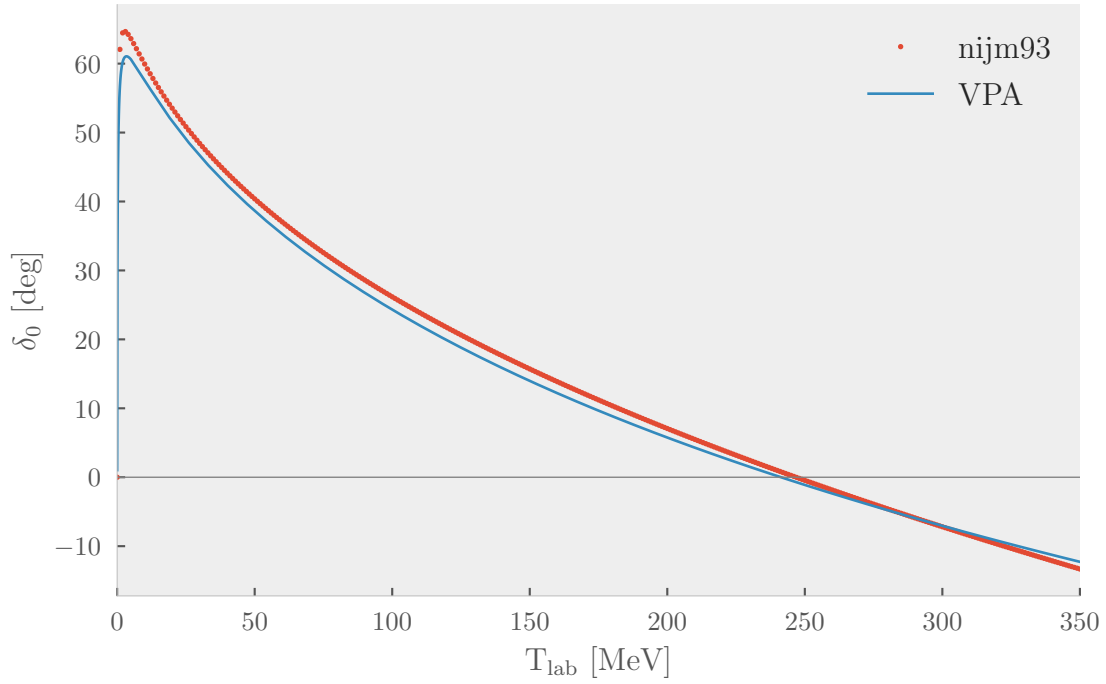
Figure 4.8: The resulting S-wave phase shift from variable phase approach alongside experimental data.
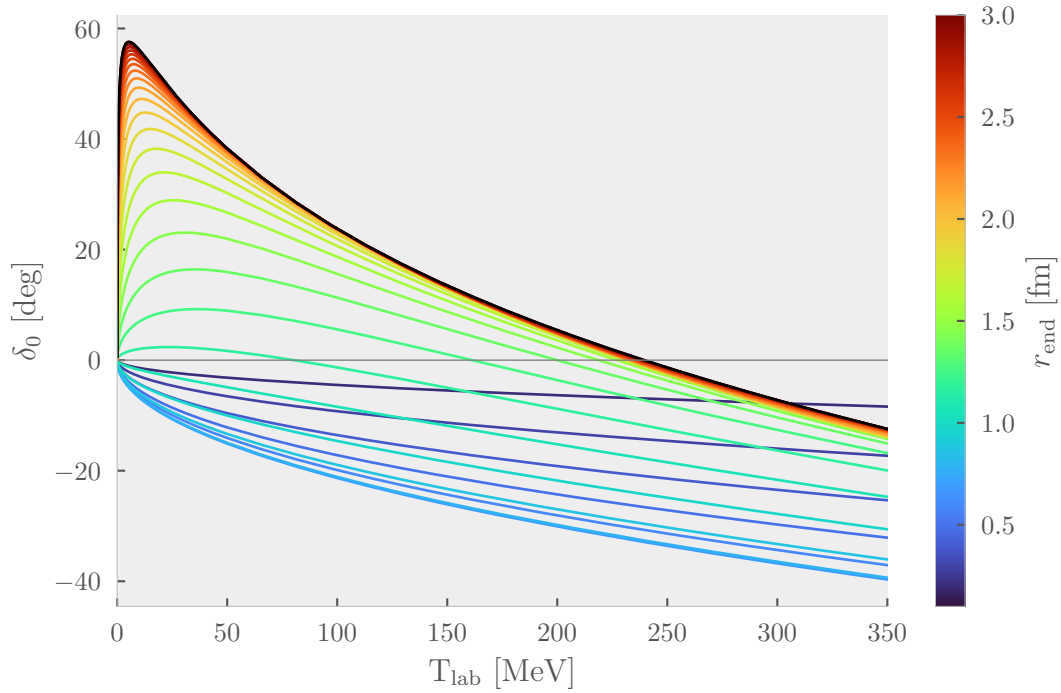

Figure 4.9: The effect of using different cut off points r_{end} of the potential. Note how the different cut off points correspond to the different radii of Fig. 2.2.
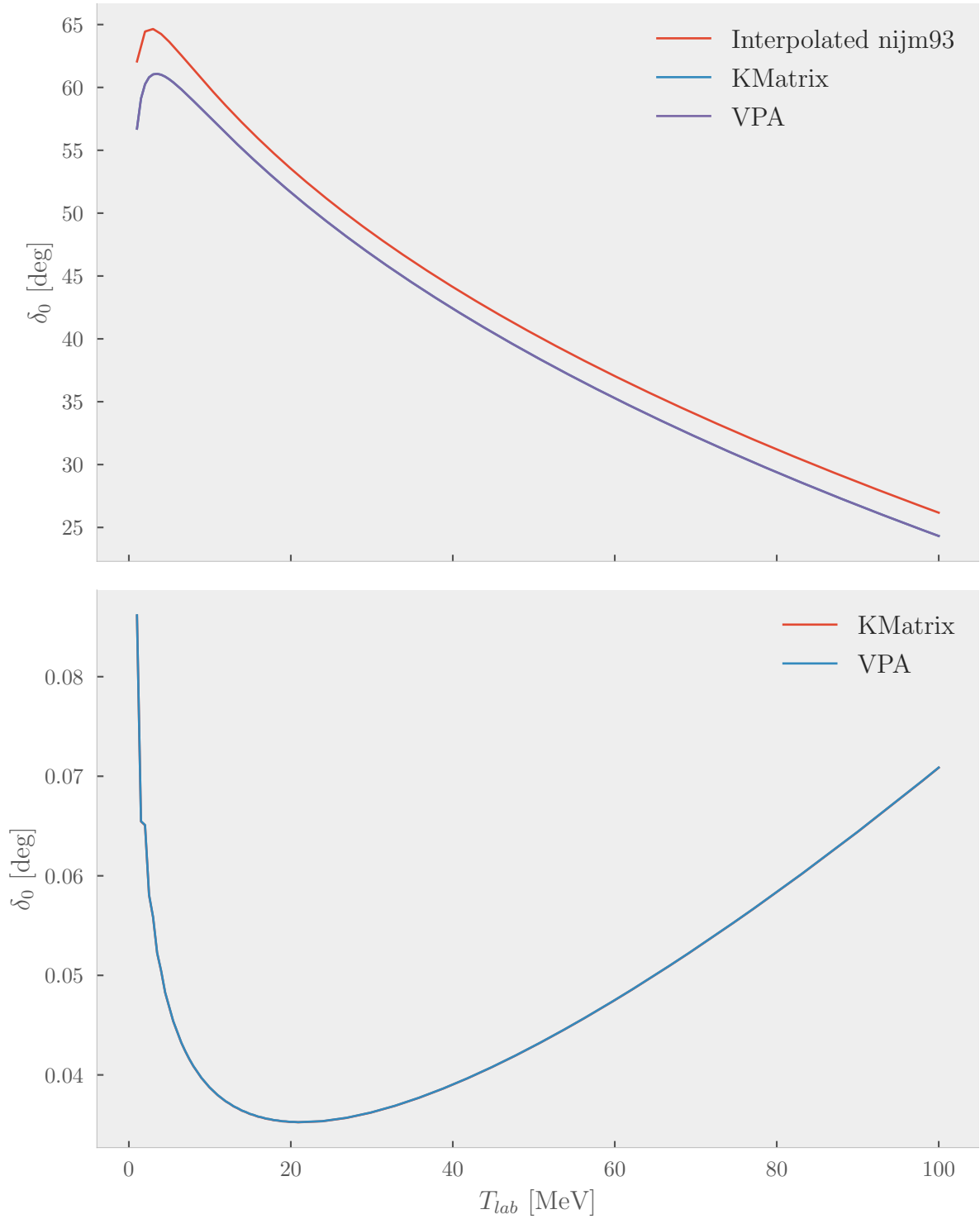
Figure 4.10: The results of K-matrix and VPA using good parameters, compared to the *nijm*93 data. The relative error is shown in the lower panel. Only $1 < T_{\text{lab}} < 100$ MeV are included; an arbitrary choice to exclude the jump at ≈ 0.1 MeV and the crossing near 250 MeV.
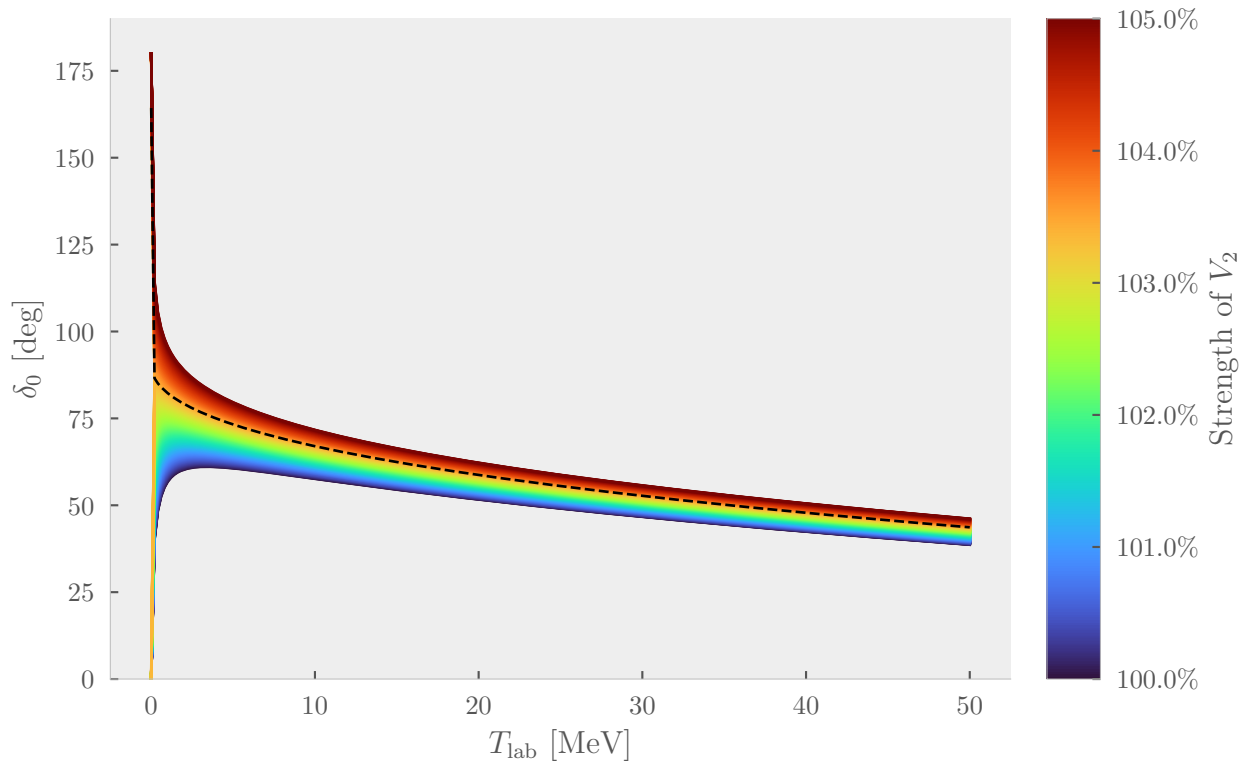
Figure 4.11: The phase shift curves resulting from making the Reid potential more attractive by increasing the strength of its second term ($V_2 = -1650.6$ MeV). The initial blue 100% denotes its original value. At a 3.37% increase, the curves no longer begin at 0°, but jump to 180°. This is marked by a dashed line. The apparent lower start point is due to numerical inaccuracy.

References

[1]   Eric C. Le Ru, Walter R. C. Somerville, and Baptiste Auguié. "Radiative correction in approximate treatments of electromagnetic scattering by point and body scatterers". In: Physical Review A 87.1 (Jan. 2013). DOI: 10.1103/physreva.87.012504. URL: https://doi.org/10.1103%2Fphysreva.87.012504 (cit. on p. 6).

[2]   Roderick V Reid. "Local phenomenological nucleon-nucleon potentials". In: Annals of Physics 50.3 (1968), pp. 411–448. ISSN: 0003-4916. DOI: https://doi.org/10.1016/0003-4916(68)90126-7. URL: http://www.sciencedirect.com/science/article/pii/0003491668901267 (cit. on p. 8).

[3]   Christopher Rackauckas and Qing Nie. "Differentialequations.jl–a performant and feature-rich ecosystem for solving differential equations in julia". In: Journal of Open Research Software 5.1 (2017) (cit. on p. 11).

[4]   R. John Taylor. Scattering Theory. John Wiley & Sons, Inc., 1972 (cit. on p. 12).

[5]   V. G. J. Stoks et al. "Partial-wave analysis of all nucleon-nucleon scattering data below 350 MeV". In: Phys. Rev. C 48 (2 Aug. 1993), pp. 792–815. DOI: 10.1103/PhysRevC.48.792. URL: https://link.aps.org/doi/10.1103/PhysRevC.48.792 (cit. on pp. 12, 17).
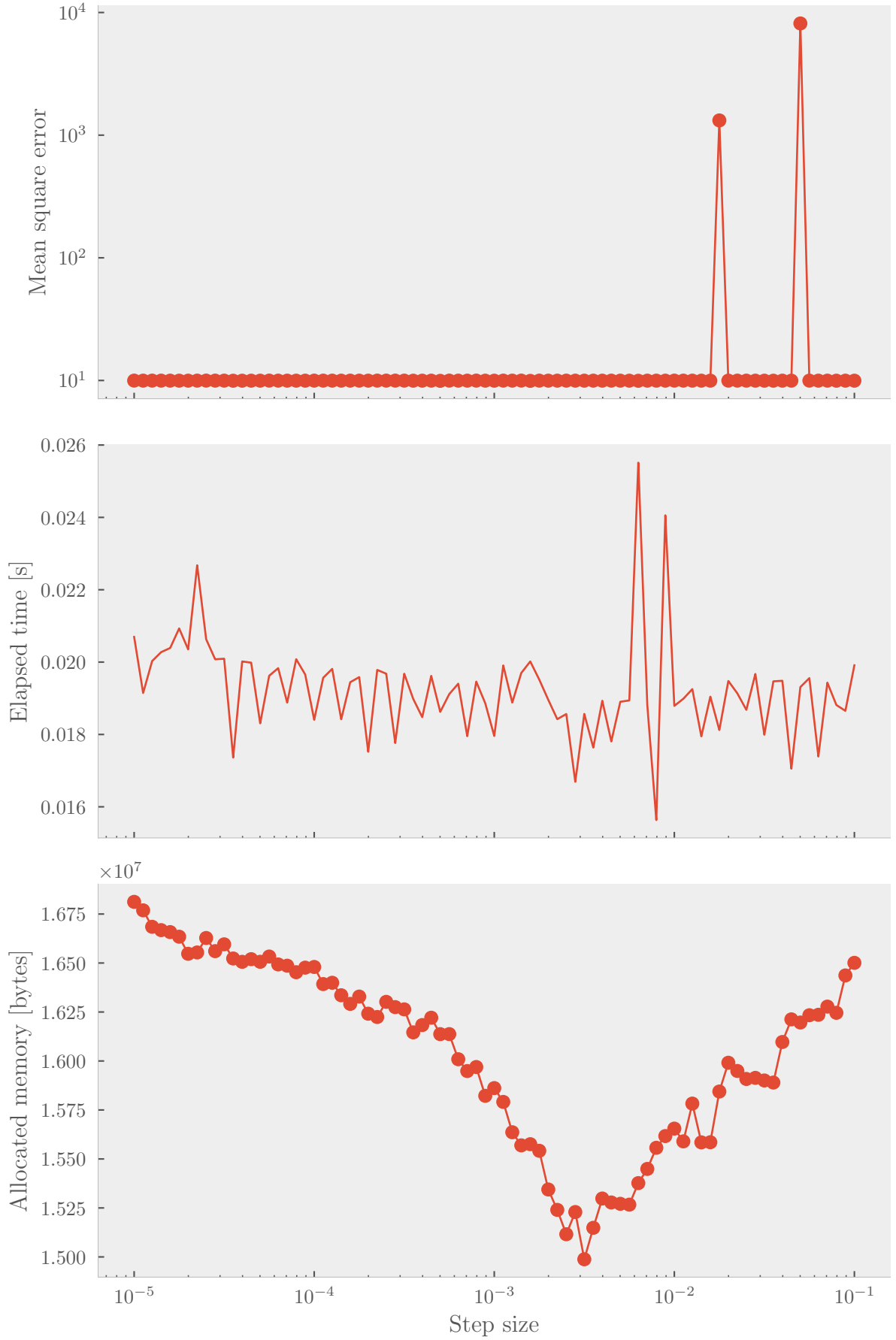
Appendices

Figure A.1: Mean square error and resource usage of VPA as a function of step size of the solver. Only allocated memory has a significant change, reaching a minimum at 0.008
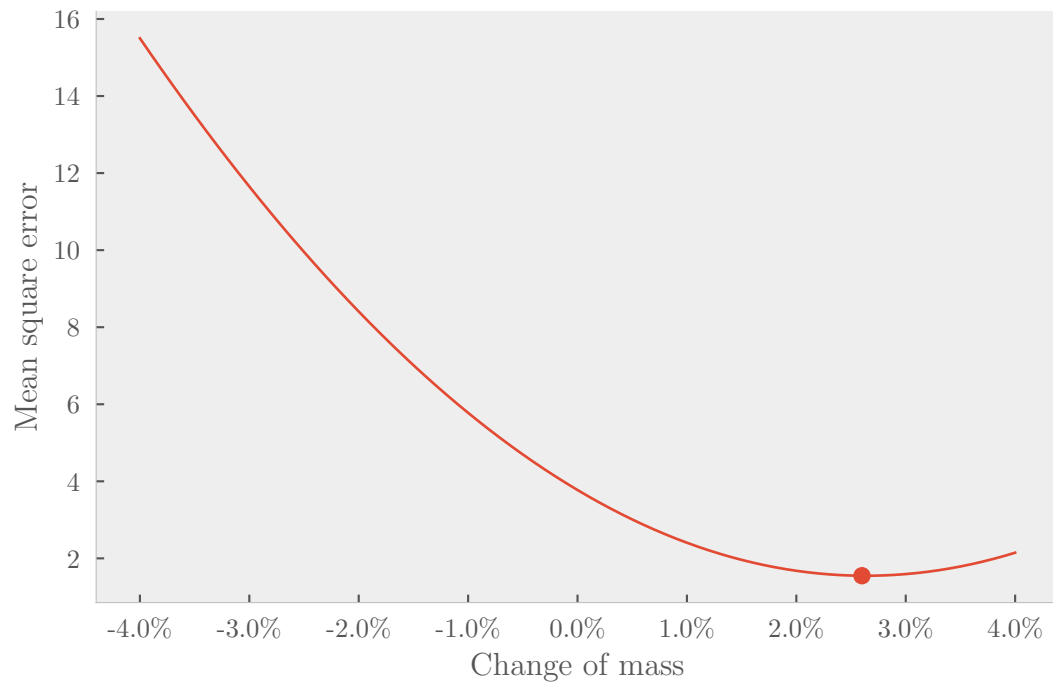
Figure B.1: The total MSE of each model using different mass. The minimum occurs at an additional $+2.6\%$ mass, $481.9\,\mathrm{MeV/c^2}$.